**Atmospheric
Chemistry
and Physics
Discussions**

In situ measurements of aerosols optical properties and number size distributions in a subarctic coastal region of Norway

S. Mogo[1,2,3], V. E. Cachorro[1], J. F. Lopez[1], E. Montilla[1,*], B. Torres[1],
E. Rodríguez[4], Y. Bennouna[1], and A. M. de Frutos[1]

[1]Universidad de Valladolid, Grupo de Óptica Atmosférica, Spain
[2]Universidade da Beira Interior, Faculdade de Ciências, Covilhã, Portugal
[3]Instituto Dom Luis, Portugal
[4]Finnish Meteorological Institute, Climate Change Unit, Helsinki, Finland
[*]now at: Universidad de Concepción, Center for Optics and Photonics, Chile

Discussion Paper

Discussion Paper

Discussion Paper

Discussion Paper

ACPD

11, 32921–32964, 2011

SSA in the ALOMAR station

S. Mogo et al.

Title Page

Abstract	Introduction
Conclusions	References
Tables	Figures

◀◀   ▶▶

◀   ▶

Back   Close

Full Screen / Esc

Printer-friendly Version

Interactive Discussion

Abstract

In situ measurements of aerosol optical properties were made in the summer of 2008 at the ALOMAR station facility (69°16 N, 16°00 E), located at a rural site in the north of the island of Andøya (Vesterålen archipelago), approximately 300 km north of the Arctic Circle. The extended three-month campaign was part of the POLARCAT Project (Polar Study using Aircraft, Remote Sensing, Surface Measurements and Models, of Climate, Chemistry, Aerosols, and Transport) of the International Polar Year (IPY-2007-2008). Its goal was to characterize the aerosols of this sub-Arctic area, which are frequently transported to the Arctic region. The ambient light-scattering coefficient, σ_s (550 nm), at ALOMAR had a measured hourly mean value of 5.41 Mm^{-1} (StD = 3.55 Mm^{-1}), and the light-absorption coefficient, σ_a (550 nm), had a measured hourly mean value of 0.40 Mm^{-1} (StD = 0.27 Mm^{-1}). The scattering/absorption Ångström exponents, $\alpha_{s,a}$, are used for a detailed analysis of the variations of the spectral shape of $\sigma_{s,a}$. Whereas α_s demonstrates the presence of two particle sizes corresponding to two types of aerosols, the α_a demonstrates only one type of absorbing aerosol particles. Values of α_a above 1 were not observed. The single-scattering albedo, ω_0, ranged from 0.62 to 0.99 (mean = 0.91, StD = 0.05), and the relationships of this property to the absorption/scattering coefficients and the Ångström exponents are presented. The concentration of the particles was monitored using a scanning mobility particle sizer (SMPS), an aerodynamic particle sizer (APS) and an ultrafine condensation particle counter (UCPC). The shape of the median size distribution of the particles in the submicrometer fraction was bimodal, and the submicrometer, micrometer and total concentrations presented hourly mean values of 1277 cm^3 (StD = 1563 cm^3), 1 cm^3 (StD = 1 cm^3) and 2463 cm^3 (StD = 4251 cm^3), respectively. The modal correlations were investigated, and the concentration of particles sized between 30 and 100 nm (Aitken mode) are presented as a function of the concentration of the particles sized between 100 and 390 nm (accumulation mode). The optical and the microphysical parameters are related to each other, and the results are presented. The origins and pathways of air

masses were examined by computing the back-trajectories in a trajectory model (HYS-PLIT). Six geographical sectors were defined to classify the air masses, and, based on the sector classification, the linkage between the air mass origin and the optical parameters was established. Aerosol size distributions were also evaluated in relation
5 to the air masses. The relationships between the air mass origins and other parameters, especially those related to the single scattering albedo, allow us to describe two characteristic situations: northern and western air masses, which had predominantly marine aerosols, presented lower optical parameter values, indicating predominantly coarser and non-absorbent particles; and eastern and southern air masses, in which
10 continental aerosols were predominant, presented higher values for all optical parameters, indicating the presence of smaller absorbent particles.

1 Introduction

The net effect of aerosols on global climate change is uncertain because the particles involved can cause cooling or warming, depending on their optical properties. The
15 reduction in the intensity of a direct solar beam during its propagation through the atmosphere is determined by both absorption and scattering processes. The aerosol single-scattering albedo, ω_0, is defined as the fraction of the aerosol light scattering over the extinction:

$$\omega_0 = \frac{\sigma_s}{\sigma_s + \sigma_a} \, , \tag{1}$$

20 where σ_s and σ_a are the aerosol scattering and absorption coefficients, respectively. ω_0 is one of the most relevant optical properties of aerosols, because the direct radiative effect of aerosols is very sensitive to this parameter. The optical properties of aerosol particles suspended in the atmosphere are determined by their chemical composition, size, shape, concentration and state of mixing and generally exhibit great spatial and
25 temporal variability (Kokhanovsky, 2008).

Sulfate and nitrate aerosols from anthropogenic sources are considered the primary particles responsible for net cooling. They scatter solar radiation and are effective as cloud condensation nuclei that affect cloud longevity and the hydrological cycle and result in a negative radiative forcing that leads to a cooling of the Earth's surface. To some extent, sulfate and nitrate aerosols are thought to counteract global warming caused by greenhouse gases such as carbon dioxide (Boucher and Haywood, 2001). Sea-salt and non-sea-salt sulfate have been reported as dominating the light scattering effect in the Arctic (Quinn et al., 2002). Previous papers studying the Arctic have also reported the occurrence of large concentrations of biogenic scattering aerosols derived from the oxidation of atmospheric dimethylsulfide, which results from oceanic phytoplankton processes (Quinn et al., 2002). It has also been suggested that the organic species play important roles in aerosol light scattering (Quinn et al., 2002) and are an important component in general of Arctic aerosols (Quinn et al., 2002; Ricard et al., 2002a,b; Leck and Bigg, 2005).

On the other hand, light-absorbing particles, mainly formed by black carbon produced by the incomplete combustion of carbonaceous fuels, are effective absorbers of solar radiation and have the opposite effect, i.e., they warm the atmosphere. Absorption of solar radiation by aerosols causes heating of the lower troposphere, which may lead to altered vertical stability and has implications for the hydrological cycle (Ramanathan et al., 2001). In addition, the deposition of light-absorbing particles onto snow and ice reduces the surface albedo, which, in turn, affects the snow pack and the Earth's total albedo (Law and Stohl, 2007; IPCC, 2007). Clarke and Noone (1985) found that snow albedo is reduced by 1–3 % in fresh snow and by a factor of 3 as the snow ages and the light-absorbing particles become more concentrated. The Arctic summer provides an excellent environment for studying remote background aerosols, as there are few sources of natural particles and few local sources of anthropogenic particles.

Data can only be retrieved from satellites operating in clear sky conditions and are mainly valid over dark targets; few satellites retrieve valid data over bright land and

SSA in the ALOMAR station

S. Mogo et al.

Title Page

Abstract	Introduction
Conclusions	References
Tables	Figures

|◄ | ►|

◄ | ►

Back | Close

Full Screen / Esc

Printer-friendly Version

Interactive Discussion

snow/ice surfaces. In addition, the optical properties of aerosols are much more variable at the Earth's surface than at the top of the atmosphere, making the estimations much more difficult (Li et al., 2007). Whereas columnar aerosol properties have been studied (Toledano et al., 2006), no surface measurements appear to have been reported on these important optical properties of aerosols in the area of our study.

In addition, measurement of the numerical size distribution can be used to infer the aerosol sources. For example, the presence of coarse modes can be due to mechanical generation processes, and the presence of ultrafine modes can be due to the formation of new particles. For a given location, this information is useful for understanding the local aerosol and its relation to the sampled air mass. Previous works (Birmili et al., 2001; Tunved et al., 2005) have observed that different size distribution properties are related to the origin of the air masses.

This study was conducted within the framework of a larger intensive aerosol characterization campaign conducted in Northern Norway at a remote subarctic site in the summer of 2008. The main goal of the campaign was to comprehensively characterize the local aerosols, and the campaign was conducted by the Atmospheric Optics Group of Valladolid University as part of the International Polar Year through the POLARCAT project. Several instruments for aerosol characterization were employed simultaneously: the aerosol radiative properties were examined using a particle soot absorption photometer (PSAP) and a nephelometer; a scanning mobility particle sizer (SMPS) and an aerodynamic particle sizer (APS) were used to obtain the numerical size distribution in the fine and coarse particle fractions, respectively; an ultrafine condensation particle counter (UCPC) was used to obtain the total concentration of the particles; and a cascade impactor with four stages allowed for independent determination of absorption coefficients using an integrating sphere technique (Montilla et al., 2011). Finally, we must mention that the measurement site belongs to the AERONET network, and hence, the columnar aerosol data are also readily available (Rodríguez et al., 2011) and were used as complementary information.

Title Page

Abstract | Introduction

Conclusions | References

Tables | Figures

◄ | ►

◄ | ►

Back | Close

Full Screen / Esc

Printer-friendly Version

Interactive Discussion

In the present study, the results from aerosol absorption and scattering measurements and the numerical size distributions are presented. We analyze the absorption/scattering coefficients and their Ångström exponents, α_a, α_s, together with the single-scattering albedo. The Ångström exponents are described using an exponential fit, λ^α, which describes the dependence of the optical parameters on the wavelength. The determination of optical parameters as a function of wavelength is useful to distinguish between various aerosol types. For example, Rosen et al. (1979) measured $\alpha_a = 1.0$ for urban aerosol, Bond (2001) studied the spectral dependence of visible light absorption by carbonaceous particles emitted from coal combustion and found a strong spectral dependency, $1.0 < \alpha_a < 2.9$, and Mogo et al. (2005) took similar measurements at a coastal site in Southern Spain and found that $0.2 < \alpha_a < 2.0$ for the visible range of the spectrum and that $0.2 < \alpha_a < 2.5$ for the UV range. High spectral resolution data are also presented for this campaign in ALOMAR by Montilla et al. (2011). α_s can be used to infer information regarding the size of the particles as it relates inversely to particle size (Russell et al., 2010). Pereira et al. (2011) observed $\alpha_s = 1.4$ for aerosols dominated by sub-micrometer particles, and Collaud Coen et al. (2004) observed α_s to be lower than 0.5 during Saharan dust events measured at Jungfraujoch. The wavelength dependence of ω_0 is also influenced by various aerosol species. Dubovik et al. (2002) found that for urban-industrial aerosols and biomass burning, ω_0 decreases with increasing wavelength, whereas for desert dust, ω_0 increases with increasing wavelength (Collaud Coen et al., 2004). This wavelength dependence inversion can be explained by the greater size of the particles of desert dust, causing the scattering process to be dominated by geometric processes that are wavelength independent. Furthermore, some dust particles (such as hematite) are strong absorbers, and the increase of absorption together with the decrease of scattering can also contribute to the change of the slope of ω_0 from positive to negative.

2 Methods

2.1 Site description

The ALOMAR (Arctic Lidar Observatory for Middle Atmosphere Research) station is located on Andøya island close to the town of Andenes (69°16 N, 16°00 E, 380 m a.s.l.) on the Atlantic coast of Norway, approximately 300 km north of the Arctic Circle, Fig. 1. The facility is managed by the Andøya Rocket Range, and the site is well-suited for measurements of remote background aerosols due to the absence of large regional pollution sources. From the end of May to the end of July, the sun is above the horizon for 24 h each day, with a maximum elevation during the solstice of 42° at noon and 2° at midnight. The climate is strongly influenced by the Gulf Stream, which provides mild temperatures during the entire year; average temperatures are −2 °C in January and 11 °C in July. Rapid variations in temperature can occur the in summer months, from 4° to 30 °C. During our measurement period, the daily average temperature was 7.1 °C, with a minimum of 2.5 °C (15 June), a maximum of 15.4 °C (20 July) and a standard deviation of 2.9 °C. The relative humidity level was high across the study period, with an average of 92.8 %. The minimum humidity level was 62 %, the maximum humidity level was 100 % and the standard deviation was 9.0 %. The surface wind pattern was oriented mainly south-southwest (27 % of occurrences), but an east-northeast component was also frequently registered (22 %). Other frequent wind directions were south-southeast (16 %), west-southwest (15 %) and east-southeast (13 %). The average wind speed was 5.6 km h^{-1} (with a minimum, maximum and standard deviation of 2.1, 13.1 and 2.4 km h^{-1}, respectively). Further details regarding the measurement station can be found in Skatteboe (1996) and Toledano et al. (2006).

2.2 Instrumentation

Aerosol samples were obtained from a stainless steel inlet protected with a rain cap and a metal screen designed to exclude insects. The inlet of the sampling line was

Title Page

Abstract | Introduction

Conclusions | References

Tables | Figures

|◀ | ▶|

◀ | ▶

Back | Close

Full Screen / Esc

Printer-friendly Version

Interactive Discussion

approximately 2 m above the roof of the measurement station building, which was approximately 7 m above the ground. The cut-off diameter of the inlet nozzle and sample transport line was approximately 10 µm. The sample air was heated when necessary to achieve a low relative humidity of 40 % prior to entering the instruments. Airflow through the sampling line was divided into several separate flows and directed to individual instruments. The flow to each instrument was controlled once a day using an electronic bubble flowmeter (Gilibrator system, Gilian).

The light absorption coefficients were measured at three wavelengths (470, 522 and 660 nm) using a particle soot absorption photometer (PSAP, Radiance Research) at a flow set to 1.5 l min^{-1}. The instrument uses a filter-based technique in which aerosols are continuously deposited onto a glass fiber filter at a known flow rate. The change in the transmitted light is related to the optical absorption coefficient using Beer's law. The instrument is an improved version of the integrating plate method (Lin et al., 1973) and is described in detail by Bond et al. (1999) and Virkkula et al. (2005).

The scattering and backscattering coefficients were measured at three wavelengths (450, 550 and 700 nm) using an integrating nephelometer (model 3563, TSI) at a flow rate of 46 l min^{-1}. The instrument is described in detail by Anderson et al. (1996) and Anderson and Ogren (1998). Calibration was conducted twice per month using CO_2 as the high-span gas and filtered air as the low-span gas. The averaging time was set to 1 min. The zero signal was measured once per hour. The data was corrected for truncation errors according to Anderson and Ogren (1998). For the 1-min averages, the detection limits for the scattering coefficients were 0.65, 0.25 and 0.38 Mm^{-1} for 450, 550 and 700 nm, respectively (Anderson et al., 1996).

The numerical size distributions of dry particles were measured separately for the fine and coarse fractions using a scanning mobility particle sizer (SMPS) and an aerodynamic particle sizer (APS, model 3321, TSI), respectively. The SMPS consists of a differential particle size classifier (model 3080, TSI) and a condensation particle counter (model 3022A, TSI) and was operated at a flow rate of 1.5 l min^{-1}; the number of particles in the size range ~ 10–390 nm (mobility diameter) were detected. The

APS was operated at a flow rate of $5 \, \mathrm{l \, min^{-1}}$, and it was set up to detect the number of particles in the size range from 0.5 up to 20 µm (aerodynamic diameter). However, our inlet system had a cut-off diameter of 10 µm. The total particle concentration in the range 3–10 000 nm was monitored using an ultrafine condensation particle counter (model 3776, TSI). According to the manufacturer, this instrument detects particles as small as 2.5 nm. It was operated in high-flow mode ($1.5 \, \mathrm{l \, min^{-1}}$) to minimize diffusion losses.

The upper boundary of the size range for the SMPS data was selected to be 390 nm to achieve a better resolution for the lower particle size channels to study possible nucleation events. This option prevented us from merging the SMPS and the APS data because of the gap between the upper channel of the SMPS, 390 nm, and lower channel of the APS, 500 nm.

2.3 Data processing

The response of the PSAP depends on the loading of particles on the filter, the amount of light scattered by the particles, the flow rate and the spot size (Bond et al., 1999; Virkkula et al., 2005). The data were corrected for these dependencies using the procedure described by Bond et al. (1999). The averaging time used was 60 s, and the filter was replaced whenever the amount of transmitted light reached 70 % of the initial intensity. As the algorithms presented by Bond et al. (1999) and Virkkula et al. (2005) agreed with the higher ω_0 and the smaller σ_a, and as no other values of $\sigma_a > 6 \, \mathrm{Mm^{-1}}$ were observed at ALOMAR during the measurements, there was no need to apply the correction procedure proposed by Virkkula et al. (2005).

The corrected aerosol absorption coefficients at 470, 522 and 660 nm were extrapolated to the working wavelengths of the nephelometer, i.e., 450, 550 and 700 nm.

We prefer not to present the backscattering results, as the values obtained were below the error threshold.

To investigate the wavelength dependence of $\sigma_{a,s}$, we calculated the absorption/scattering Ångström exponent. This parameter is commonly used when conducting a more detailed analysis of the variations of the spectral shape of $\sigma_{a,s}$ and is defined as the negative slope of the logarithm of the absorption coefficient as a function of wavelength. It is given by:

$$\sigma_{a,s} = K \lambda^{-\alpha_{a,s}} . \tag{2}$$

In practice, we calculated $\alpha_{a,s(\lambda_1,\lambda_2,...,\lambda_n)}$ for more than two wavelengths through the logarithmic fit of Eq. (2), and we calculated $\alpha_{a,s(\lambda_1,\lambda_2)}$ for a pair of wavelengths, λ_1, λ_2, according to the following simplified formula:

$$\alpha_{a,s} = -\frac{\log(\sigma_{a,s}(\lambda_2)/\sigma_{a,s}(\lambda_1))}{\log(\lambda_2/\lambda_1)} . \tag{3}$$

The aerosol size distribution observations were made on the timescale of minutes, and twelve measurements were conducted per hour. For the SMPS, we describe the total concentration and the concentrations N_{30-50}, N_{50} and N_{100} as follows:

$$N_{30-50} = \sum_{30}^{50} n_i ; \quad N_{50} = \sum_{50}^{390} n_i ; \quad N_{100} = \sum_{100}^{390} n_i \tag{4}$$

where n_i is the measured aerosol number concentration in the size interval considered. The cut-off diameters of 30, 50 and 100 nm were selected according to the criteria presented by Asmi et al. (2011). The nucleation, Aitken and accumulation modes are also fully described. For the APS, we describe the shape of the distribution and the total concentration. For the UCPC instrument, the total concentration is presented.

Data from 13 June to 26 August, 2008 were available. The statistical data for all instruments were calculated based on the hourly averages, which appeared reasonable given the low values observed. The hourly averages were preferred to the daily averages because they were more sensitive to local effects, whereas the daily averages were more useful in identifying external long-range effects. The hourly value was

accepted when six or more 5-min values were available. The overall data coverage was approximately 72 % due to the weather conditions, and this value is considered adequate for determining the main features of optical properties and concentrations of the aerosols.

3 Results and discussion

3.1 Temporal variations in aerosol optical properties

The aerosols sampled at ALOMAR during the 2008 summer campaign were representative of an extremely clean area. During our observations, hourly mean σ_s at 450, 550 and 700 nm ranged from 0.29 to 31.24 Mm^{-1}, 0.25 to 23.21 Mm^{-1} and 0.19 to 18.95 Mm^{-1} (average 7.31, 5.41 and 4.08 Mm^{-1} with standard deviations of 4.79, 3.55 and 2.84 Mm^{-1}), respectively. The hourly mean values of σ_a at 450 nm, 550 nm and 700 nm ranged from 0.14 to 2.72 Mm^{-1}, 0.13 to 2.28 Mm^{-1} and 0.12 to 1.92 Mm^{-1} (average 0.45, 0.40 and 0.36 with standard deviations of 0.33, 0.27 and 0.23 Mm^{-1}), respectively. For both parameters, the median value was lower than the mean. The range of the values of σ_s was ten times larger than the range of the values of σ_a. Statistical data regarding the σ_s and σ_a values are presented in Table 1, and a time series representing over 70 days of measurement is shown in Fig. 2.

1166 hourly means were available for σ_s, and 1046 were available for σ_a, which allowed for the calculation of 883 hourly values of ω_0. The frequency histogram of σ_s, σ_a and ω_0 at 550 nm, shown in Fig. 3, presents only one frequency mode, centered at 3 Mm^{-1}, 0.3 Mm^{-1} and 0.95, respectively, for each parameter. Although the magnitude of σ_s and σ_a depend on many factors, our results, when compared with the literature values for other areas and Table 1, suggest that the magnitude of the aerosol scattering/absorption coefficients at ALOMAR were comparable to those in other polar regions, such as those presented by Delene and Ogren (2002) and Quinn et al. (2007) at Barrow and Aaltonen et al. (2006) at Pallas.

SSA in the ALOMAR station

S. Mogo et al.

Title Page

Abstract	Introduction
Conclusions	References
Tables	Figures

◄◄ ►►

◄ ►

Back Close

Full Screen / Esc

Printer-friendly Version

Interactive Discussion

Correspondingly, the hourly mean values of the ω_0 parameter measured at ALOMAR presented average values of 0.93, 0.91 and 0.89 at 450 nm, 550 nm and 700 nm, respectively. Values ranged from 0.60 to 0.99, 0.62 to 0.99 and 0.50 to 0.99, respectively (see Fig. 2 and Table 1). The lowest value registered was 0.62 (550 nm); but, in fact, ω_0

5   was observed to vary mainly between 0.80 and 0.99, as seen in Fig. 2 and confirmed by the value of the median, 0.92, and the P_{25}, 0.89 (550 nm) (see also Fig. 3). These values lie in the range presented for polar regions by several authors as compiled by Tomasi et al. (2007).

    The measured spectral series of σ_s and σ_a were used to derive the corresponding

10   values of the scattering and absorption Ångström exponents following the best-fit procedure based on Eq. (2). The Ångström exponents calculated for the 450 nm/700 nm wavelength pairs lay in the range between 0.20 and 3.07 for scattering and in the range between 0.01 and 0.97 for absorption. The observation of α_a values below 1 are an interesting characteristic of the local absorbent particles and has previously been pre-

15   sented by Montilla et al. (2011). Statistical properties of the hourly mean values of the calculated parameters are presented in Table 1 and show mean values of 1.37 and 0.40, respectively. In both cases, the median value is lower than the mean. The standard deviations are 0.61 and 0.21, respectively. Figure 4a shows the hourly mean Ångström exponent values for the 450 nm/700 nm wavelength pair covering the entire

20   measurement period.

    The frequency histograms of α_s and α_a are shown in Fig. 4b,c. The histogram for α_a presents only one frequency mode, centered at 0.35, whereas the histogram for α_s presents two modes, centered at 0.7 and 1.9. Whereas the absorption Ångström exponent lies in the range presented for other polar regions (Tomasi et al., 2007; Aaltonen

25   et al., 2006), the scattering Ångström exponent presents a few high values that are more typical of sites affected by urban or continental pollution (Vrekoussis et al., 2005; Lyamani et al., 2008). These values may be due to long-range transport episodes from Southern Europe.

We also analyzed the spectral dependence of the single-scattering albedo because this parameter, α_{ϖ_0}, is known to be very sensitive to the composition of the particles. For the 450 nm/700 nm wavelength pair, α_{ϖ_0} was found to range between −0.11 and 0.95 (with a mean value and a standard deviation of 0.09). The high standard deviation of this parameter within its range of values indicates that a large variety of aerosol types is present at ALOMAR during the summer. The observed negative values are due to desert aerosol air masses that reach the ALOMAR station. These rare events are usually weak and of short duration because desert aerosols have to travel across Europe to reach the ALOMAR station. One or two of these events, of 1–2 days in duration, are observed every summer (Rodríguez et al., 2011). These events were confirmed by data from the CIMEL sun photometer (part of the AERONET network) located at the station. Back trajectories and MODIS images were analyzed and also confirmed the dust events.

3.2 Particle number concentrations in various size ranges

In this section, we first independently present the characteristics of each particle size range and then analyze the relations between these ranges.

The average hourly concentration for the submicrometer particles (10–390 nm) was 1277 cm^{-3}, with a standard deviation of 1563 cm^{-3}. The average value for the concentration of micrometer-sized aerosols (0.5–10 µm) was 1 cm^{-3}, with a standard deviation of 1 cm^{-3}. The average number concentration measured for the total range (3–10 000 nm) is 2463 cm^{-3}, with a standard deviation of 4251 cm^{-3}. The submicrometer range is further investigated for the ranges 30–50, 50–390 and 100–390 nm. The average number concentrations and their standard deviations are 258 cm^{-3} (355 cm^{-3}), 469 cm^{-3} (516 cm^{-3}) and 183 cm^{-3} (209 cm^{-3}), respectively. The concentration percentiles are tabulated with their respective mean values in Table 2. ALOMAR has slightly higher results for the aerosol number concentration in the size sections N_{30-50} and N_{50} but slightly smaller concentrations for N_{100} than those measured in the sampling study of Asmi et al. (2011) conducted at the Pallas station, which is located at

almost the same latitude as ALOMAR but at a remote continental area in Northern Finland. However, our concentration N_{100} comprises the size range 100–390 nm, whereas that of Asmi's comprises the size range 100–500 nm; therefore, the slightly smaller value for N_{100} registered in ALOMAR may not be a fair comparison. The numerical size distribution level exhibits the same range of values for the section N_{30-50} at ALOMAR as at Birkenes, which is located in Southern Norway, but the values recorded at Birkenes for N_{50} and N_{100} are almost double those registered at ALOMAR. However, the numerical size distributions across all sections at the Arctic station of Zeppelin, located in the Svalbard Islands, are half of the values recorded at ALOMAR.

A plot of the particle numerical size distributions measured for the submicrometer particles is presented in Fig. 5 and illustrates the temporal evolution for all campaign days. On the same figure, we also show the aerosol numerical concentrations of nucleation, Aitken and accumulation mode particles (30 nm and 100 nm are used as the cut-off values of the diameters between the modes). It is possible to identify three types of periods that are connected to the weather conditions: (1) clean conditions with very low concentrations of particles, usually associated with periods after rain; (2) periods with a small increase in the total concentration and rapid variations of the concentrations; and (3) periods when nucleation events occur, typically associated with sunny days with higher temperature and lower humidity.

The six-day period from 27 June to 2 July was selected for further analysis because it exemplifies the first situation, "clean conditions". In the days preceding this period, it had rained, and after the rain stopped, the nucleation, Aitken and accumulation mode concentrations presented average values of 176, 443 and 239 cm^{-3}, respectively. These measures were considered the background values for the ALOMAR station.

The period from 28 July to 1 August exemplifies of the second situation described. Very rapid variations in the numerical concentrations were observed during this period, with the three modes maintaining the high mean values of 1186, 647 and 460 cm^{-3}, respectively.

SSA in the ALOMAR station

S. Mogo et al.

The observed nucleation events caused the total particle concentration to increase from several hundred particles cm^{-3} to over 1000 particles cm^{-3}. The criteria for identifying nucleation events are based upon observations of the rapid growth of particles from 10 nm to larger sizes in a relatively short time, forming a banana-shaped growth curve in the surface plot. An example of a typical particle formation event measured at ALOMAR took place on 20 July. At 7:00 UTC, newly formed particles with diameters of less than 30 nm increased in numerical concentration until the nucleation mode reached 3912 cm^{-3}. After that value had been achieved, the particles grew at a rate of a few nm h^{-1}, reaching sizes of between 30 and 100 nm by evening and sizes larger than 100 nm by nightfall. The Aitken mode reached a maximum of 2580 cm^{-3} at 17:00 UTC, and the accumulation mode reached a maximum of 928 cm^{-3} at 01:00 UTC on 21 July.

The median size distribution for all campaign days is presented in Fig. 6, showing the median, 16th and 84th percentiles of each measured size section. A bimodal shape is observed for the submicrometer fraction. The Aitken mode, which is rather flat for diameters from 40 to 50 nm, has a maximum concentration of 627 cm^{-3}. The accumulation mode occurs for diameters from 140 to 170 nm and has a maximum concentration of 260 cm^{-3}. The APS data show a small mode at 3300 nm for the coarse fraction, Fig. 6b. The ratio between the Aitken and accumulation modes, N_{30-100}/N_{100}, remained mostly above 1 throughout the campaign, ranging from 0.15 to 161.52, with an average of 4.47 (StD = 7.67). The relation between the Aitken and the accumulation modes was investigated by examining the concentration of particles between 30 and 100 nm as a function of N_{100} concentrations, Fig. 7. The N values are concentrated mainly in a grouping between 100 and 1000 cm^{-3}. According to Asmi et al. (2011), the shape of the scatter density contour can be interpreted as a characteristic feature of the station, and comparison of our findings with their work demonstrates that the data from ALOMAR presents similar behavior to those of the other Nordic stations.

Further comparison of the aerosols at the ALOMAR station with other Nordic stations yields several other similarities. The size distribution presents a bimodal median

distribution in the submicrometer fraction for ALOMAR and all other Arctic stations. Although the individual behavior of the particulates at the ALOMAR station has been presented with respect to the mean concentrations of particles in each size section, the particulate composition at the ALOMAR station is sufficiently similar to that at other
5 Nordic stations (considered in Asmi et al., 2011) to include it in the group "Northern European Aerosol".

3.3 Relationships between the aerosol parameters

In Fig. 8a,c, we present the correlation between scattering/absorption in the various channels. The relation between channels describes the proportion of the measure-
10 ments at different wavelengths, and each pair of measurements should obey Eq. (2). In this way, the slope of the linear fit for each correlation is the respective Ångström exponent. For the absorption coefficients, one line is sufficient to correlate the different channels, but two lines with different slopes are observed for the scattering coefficients. The slopes of these lines depend on the particle size; therefore, these two lines appear
15 to represent different aerosol types, and the Ångström exponent can be used to help identify the aerosol types. The line with smaller slope is associated with larger particles and marine aerosols. The data that contribute to this line have a strong correlation with the numerical concentrations of the coarse particles $N_{micrometer}$ (> 500 nm) as demonstrated by the value $R = 0.9$. The line with the higher slope is associated with smaller
20 particles, i.e., continental or polluted aerosols, and its data present a correlation of $R = 0.6$ with the concentration of particles in the accumulation mode, N_{100}.

Additionally, in Fig. 8b,d, we present the relation between the scattering/absorption coefficients and the respective Ångström exponents. The Ångström exponents were calculated for the pairs of wavelengths 450 nm/550 nm ($\alpha_{a,s}$ (450–550)),
25 550 nm/700 nm ($\alpha_{a,s}$ (550–700)) and 450 nm/700 nm ($\alpha_{a,s}$ (450–700)), and for the three wavelengths 450 nm/550 nm/700 nm ($\alpha_{a,s}$ (450–550–700)). For both scattering and absorption cases, the Ångström exponents are higher for the pair of wavelengths 450 nm/550 nm and smaller for the pair 550 nm/700 nm, thereby defining the shape of

the scattering and absorption spectra in the following way: decreases quickly in the 450 nm/550 nm range and decreases less abruptly in the 550 nm/700 nm range. For the Ångström exponents calculated, we determined the fit error, e, and the quality of the fit using the R parameter. The fit error was calculated as the standard error of the slope of the best-fit line for the observed data $\sigma \times \lambda$; its mean value is 23 %. The R parameter was computed as the fraction of the total variation of the σ values of data points that are attributable to the assumed fitting line and was only used qualitatively to evaluate the fit. Both e and R were used to evaluate and filter the data set.

Figure 9a illustrates the relation between the scattering and the absorption coefficients. This represents another way to analyze the single-scattering albedo parameter. In Fig. 9b, the relation between the Ångström exponents is also presented, and two regions can be identified as exhibiting a higher density of data. Region A, which has higher exponents due to the presence of fine particles, may originate from continental urban sources. Region B, which has lower exponents due to he presence of coarse particles, which are clean and less absorbent, may be of marine origin. These two regions represent the two modes that were observed in the frequency histogram of the α_s parameter, Fig. 4b. Note the higher density around $\alpha_s = 0.7$ and $\alpha_s = 1.9$ and the lower density around $\alpha_s = 1.3$.

Figure 10 displays the value of ω_0 as a function of the scattering/absorption coefficients and the Ångström exponents. For a given σ_a value, lower ω_0 values correspond to smaller particles, and higher ω_0 values correspond to larger particles (Clarke et al., 2007). Additionally, the fine particles are present in the more absorbent region whereas the coarse particles are present in the less absorbent region. The particle size can be indicated by the scattering Ångström exponent, with higher values of α_s for smaller particles and smaller values of α_s for larger particles. In this way, the relationship between ω_0, an intensive aerosol optical property, and σ_a, an extensive property, can be used to differentiate between background aerosols and the inputs of primary aerosols (Cappa et al., 2009). At the ALOMAR station, we observe predominantly high values of ω_0 due to the very low σ_a values. This fact, together with the α_s values registered, allows us

to describe the local air as extremely clean and only episodically influenced by small particles resulting from long-range transport. This conclusion is also supported by the results of other techniques such as the analysis of the origin of air masses (see Sect. 3.4) and the use of MODIS images and columnar data from the CIMEL photometer (not shown) (Rodríguez et al., 2011).

In Fig. 10e, the single-scattering albedo, ϖ_0, is plotted against its own exponent, α_{ϖ_0}. The spectral shape decreases mainly with the wavelength, $\alpha_{\varpi_0} > 0$, but in some cases the single scattering albedo increases with the wavelength ($\alpha_{\varpi_0} < 0$) due to the arrival of dust (Rodríguez et al., 2011). These cases were characterized by higher total particle numerical concentrations, such as 3919 cm^3.

Figure 11a,b illustrates the particle numerical concentration in different size fractions and modes as a function of the scattering coefficient (550 nm). Based on the Mie theory, only the micrometer fraction and the accumulation mode are expected to present strong correlations with σ_s, whereas the scattering coefficient is expected to be unresponsive to the ultrafine mode (nucleation + Aitken). In our results, no clear connection between the total particle numerical concentration and the scattering coefficient can be seen. However, if we look at specific size ranges, we see that aerosol particle concentration in the coarse mode is strongly correlated ($R = 0.9$) with the scattering coefficient. This correlation is lower for the numerical concentration of accumulation mode particles ($R = 0.5$). No correlation can be seen for the Aitken and nucleation modes. These results are consistent with those presented by Aaltonen et al. (2006) at the Pallas station, who reported correlations of 0.71 for the coarse fraction and 0.60 for the accumulation mode. However, care should be taken when directly comparing the accumulation mode results, as Aaltonen et al. (2006) considered the range 95–500 nm, whereas our accumulation mode results are for the range 100–390 nm. It was also previously shown by Virkkula et al. (1998), using results recorded in Finnish Lapland, that the correlation between the total particle numerical concentration and σ_s is low, but the correlation between the numerical concentration in the accumulation mode and σ_s is high.

SSA in the ALOMAR station

S. Mogo et al.

Title Page

Abstract | Introduction

Conclusions | References

Tables | Figures

◄ | ►►

◄ | ►

Back | Close

Full Screen / Esc

Printer-friendly Version

Interactive Discussion

The relationship between the particle size distributions and the scattering Ångström exponent is presented in Fig. 11c,d. The size of the particles is expressed as the count mean diameter of the size distribution, CMD $= \frac{\sum (d_p)_i N_i}{N}$, the surface mean diameter, SMD $= \frac{\sum (d_p)_i S_i}{S}$ (not shown) and the volume mean diameter, VMD $= \frac{\sum (d_p)_i V_i}{V}$. For the submicrometer fraction, the value of α_s is insensitive to the size distribution. The correlation coefficients are 0.19, -0.04 and -0.06 for CMD, SMD and VMD, respectively. For the micrometer fraction, the value of α_s is correlated most strongly with the CMD. The fits are -0.70, -0.12 and 0.10 for CMD, SMD and VMD, respectively. In the studies by Virkkula et al. (1998) and Garland et al. (2008), it was observed that the correlation of CMD with α_s is not as strong as the correlation of SMD and VMD with α_s. This difference occurs because the size distribution was considered as a whole in both works cited; however, in our work, the analysis is performed separately for the sub-micrometer and micrometer fractions. Consideration of all sizes biases the correlation with CMD because it gives more weight to the small particles, which are less sensitive to scattering.

The fraction of particles that contribute to each ϖ_0 value is presented in Fig. 11e, and Fig. 11f presents the size of the particles as a function of ϖ_0. In practice, Fig. 11e has the same meaning as Fig. 10a,b, as confirmed by the similar shape of the graphs. Note the similar shape between the graphs of $\varpi_0 \times \sigma_a$ and $N_{submicrometer} \times \varpi_0$, confirming that for a given value of σ_a, lower values of ϖ_0 correspond to smaller particles and higher values of ϖ_0 correspond to larger particles. Likewise, the graphs of $\varpi_0 \times \sigma_a$ and $N_{micrometer} \times \varpi_0$ also present similar shapes. In Fig. 11f, we see that for the sub-micrometer fraction, the CMD varied from ~ 20 to ~ 160 nm, with an average value of 66 nm. For the micrometer fraction, the CMD varied from ~ 500 to ~ 1400 nm, with an average value of 900 nm. Classifying the ϖ_0 into 5 bins, $\varpi_0 < 0.80$, 0.80–0.85, 0.85–0.90, 0.90–0.95 and 0.95–1.00, we observe that the average values of the CMD for the submicrometer and the micrometer fractions occurred in the bins 0.80–0.85 and 0.85–0.90, respectively. The smallest average CMD, 57 nm, typical of nucleation episodes,

SSA in the ALOMAR station

S. Mogo et al.

Title Page

Abstract	Introduction
Conclusions	References
Tables	Figures

◄	►	
◄	►
Back	Close

Full Screen / Esc

Printer-friendly Version

Interactive Discussion

was calculated in the bin $\omega_0 > 0.95$. This value is slightly higher than that presented by Virkkula et al. (2011) at the Hyytiälä station, located in Southwestern Central Finland. The highest average CMD, 1065 nm, which was typical of long-range pollution episodes, was also calculated in the bin $\omega_0 > 0.95$.

3.4 Determination of air mass origins by back trajectory analysis

To analyze the source and transport pathways of the air masses arriving at ALOMAR, a back trajectories analysis was conducted covering the period of measurement using NOAA's HYSPLIT model (Draxler and Rolph, 2003; Rolph, 2003). The back trajectories were calculated typically 120 h backwards in time at an arrival height of 500 m above ground level at 12:00 UTC. The model runs were constructed using the GDAS (Global Data Assimilation System) meteorological archive, and the vertical velocity of the model as vertical motion (3-dimensional) was selected. The altitude level of 500 m was used for the classification because this is within the boundary layer, where most of the particles are confined. However, higher altitude trajectories were also used in the investigation of the long-range transport episodes.

Figure 1 shows the demarcation of six geographical sectors of different air mass types influencing the measurement site: 1(S), 2(SE), 3(E), 4(NNE), 5(NW) and 6(W). The air mass sector classification is based on the longest residence time of the trajectories in each geographical sector. This methodology has been described in detail in previous studies (Rodríguez et al., 2011; Toledano et al., 2009).

The most frequent air masses were those from the north, sectors 4 (31 %) and 5 (27 %), and from the west, sector 6 (22 %), arriving from the ocean (see Fig. 12). Other air masses originated in the south and the east, sectors 1 (5 %), 2 (3 %) and 3 (12 %), respectively, which arrived from Europe in most cases. Rodríguez et al. (2011) found that sectors 1, 2 and 3 were related to high-pressure systems that had been located over the Scandinavian Peninsula and Siberia, resulting in sunny and dry weather over the region. Sector 4 was characterized by cold and dry air masses from the Arctic

SSA in the ALOMAR station

S. Mogo et al.

Title Page

Abstract | Introduction

Conclusions | References

Tables | Figures

|◄ | ►|

◄ | ►

Back | Close

Full Screen / Esc

Printer-friendly Version

Interactive Discussion

sea. Sectors 5 and 6 were associated with low-pressure systems, and precipitation was frequent when air masses arrived from these sectors.

Based on the sector classification of each identified transport pathway, we established a linkage between the air mass origin and the parameters we measured. Figure 12a,b, summarizes the main characteristics of the optical properties of the aerosols for the six air-mass types. The mean values of σ_a, σ_s and ϖ_0 for 550 nm and α_a, α_s and α_{ϖ_0} for the pair of wavelengths 450–700 nm are shown for each sector. The maximum mean values of σ_a and σ_s were observed for sector 2 (SE) and were 0.61 and 9.53 Mm^{-1}, respectively. The minimum mean values of σ_a and σ_s were observed for sector 4 (NNE) and were 0.29 and 3.90 Mm^{-1}, respectively. The mean ϖ_0 parameter ranges from 0.89 (when the air masses came from sector 3 (E)) to 0.94 (when the air masses came from sector 2). A similar behavior is presented by α_a and α_s, for which the maximum mean values were observed in sector 2 (0.44 and 2.01, respectively). The minimum mean value of α_a, 0.24, was observed for sector 5 (NW), whereas the minimum mean α_s, 0.79, was observed for sector 4 (NNE). The mean value of α_{ϖ_0} ranges from 0.03 for sector 4 to 0.13 for sector 1 (S).

In Fig. 12c, we illustrate how the various air masses relate to the properties of the observed aerosol size distribution. The nucleation mode occurred more often in sectors 1 and 6 (S and W), whereas the Aitken and accumulation modes presented the highest concentrations in sectors 1, 2 and 3 (S, SE and E). The micrometer fraction was present at very low concentrations in all sectors, with the highest concentration in sector 2 (SE) and the lowest concentration in sector 5 (NW). Particles in the total size range, from 3 to 10000 nm, were present in sectors 1 and 2 (S and SE) at higher concentrations; sector 3 (E) presented lower concentrations.

Figure 13 shows the median aerosol size distribution measured in the air masses. The thicker line indicates the median size distribution collected for all campaign days (identical to Fig. 6), and the colored lines indicate the size distribution associated with each of the 6 sectors considered. Sector 2 (SE) presents the most distinct shape and has the highest concentration of particles, with a peak near 100 nm. Sectors 1 and 3

Full Screen / Esc

Printer-friendly Version

Interactive Discussion

(S and E), present similar shapes, but higher concentrations are observed for sector 1. The submicrometer fractions for these three air masses are distributed monomodally. The submicrometer fractions for sectors 4, 5 and 6 (NNE, NW and W) present a bi-modal shape; higher concentrations are observed for sector 6, and lower concentra-tions are observed for sector 5. The distributions for all sectors exhibits a small peak in the micrometer fraction, near 2500 nm.

Sectors 1, 2 and 3 (S, SE and E) analyzed as a whole present higher coefficients σ_a and σ_s and higher exponents α_a and α_s. On average, these sectors contain far more accumulation mode particles and higher numerical concentrations. This situation, as with continental air, corresponds to region A, which is shown in Fig. 9b. Sectors 4, 5 and 6 (NNE, NW and W), also analyzed as a whole, present lower coefficients and lower exponents, corresponding to region B in Fig. 9b, for marine air. The size distribution of the submicrometer fraction for sectors 4, 5 and 6 is markedly bimodal, and the numerical concentrations are lower than in sectors 1, 2 and 3. A more detailed discussion, in which each sector could be further broken up into special regions and in which the characteristics of mixed air masses could be specified, would require data from longer measurement periods.

4 Conclusions

Aerosol optical properties that are relevant to direct climate forcing were investigated during the summer of 2008 summer at the ALOMAR station, located in Andøya is-land on the Atlantic coast of Norway, approximately 300 km north of the Arctic Cir-cle. The primary optical measurements made were light absorption by particle soot absorption photometry and light scattering by nephelometry. The scattering coeffi-cients were strongly variable, ranging from 0.25 to 23.21 Mm^{-1} at 550 nm, whereas the absorption coefficients, also at 550 nm, were more consistent, ranging from 0.13 to 2.28 Mm^{-1}. The mean absorption coefficient was very small, leading to higher single-scattering albedos (mean $\omega_0 = 0.91$ at 550 nm). The scattering and absorption

Title Page

Abstract | Introduction

Conclusions | References

Tables | Figures

|◀ | ▶|

◀ | ▶

Back | Close

Full Screen / Esc

Printer-friendly Version

Interactive Discussion

Ångström exponents acted similarly, with higher values from 450 to 550 nm and smaller values from 550 to 700 nm. We calculated the single-scattering albedo and obtained values ranging from 0.62 to 0.99 at 550 nm. The spectral dependence of the single scattering albedo was also analyzed. The spectral shape mainly decreased with wavelength. However, some cases were noted in which the single scattering albedo increased with the wavelength.

We analyzed the main characteristics of the microphysical properties of aerosols by determining the numerical size distributions and its parameters provided by the SMPS, APS and UCPC and by examining the aerosol evolution during the campaign that lasted almost three months; these results were typical of those obtained in summer in this region. The observed mean total numerical concentration was approximately 2463 cm^{-3}. The median numerical size distributions were obtained and compared with those from other Northern European locations. The submicrometer fraction of the aerosol particles exhibited a bimodal numerical-size distribution. The Aitken mode presented a maximum concentration of 627 cm^{-3}, and the accumulation mode presented a maximum concentration of 260 cm^{-3}. The ratio between the Aitken and the accumulation modes was also analyzed and remained mostly above a value of 1.

Basic statistical values for all optical data were presented, as were intra-data relationships and particle size distributions. The scattering coefficient correlated strongly with the numerical concentration of accumulation mode particles and more strongly with the micrometer fraction of the particles. The wavelength dependence of the scattering coefficient, α_s, was compared with the submicrometer and micrometer size distributions in terms of count mean diameters, surface mean diameters and volume mean diameters. α_s was most strongly correlated with the micrometer CMD.

A back trajectory analysis showed significant differences in the optical parameters among the maritime air masses (NNE, NW and W) and continental air masses (S, SE and E). Northern and western air masses, which contained predominantly marine aerosols, presented lower values of σ_a and σ_s, and lower values of α_a and α_s, indicating that they contained predominantly coarser and non-absorbent particles. Eastern

SSA in the ALOMAR station

S. Mogo et al.

Title Page

Abstract | Introduction

Conclusions | References

Tables | Figures

◄ | ►►

◄ | ►

Back | Close

Full Screen / Esc

Printer-friendly Version

Interactive Discussion

and southern air masses, in which continental aerosols were predominant, presented higher values for all optical parameters. This result indicates the presence of smaller absorbent particles and explains the smaller values recorded for ω_0.

Most of the parameters measured at and calculated for this site are similar to those of other northern areas. Interest in this data relies on the previously unavailable variety of information for this area, which allowed us to determine the general characteristics of local aerosols for the first time. Finally, we would like to point out that this study, which was conducted using a small data set representing measurements recorded over nearly three months, allowed us to clearly distinguish between two aerosol types characteristic of defined situations. The same work, if conducted over a larger (preferable year-long) data set, would allow for more aerosol situations, in ALOMAR and other measurement sites, to be distinguished.

References

Aaltonen, V., Lihavainen, H., Kerminen, V.-M., Komppula, M., Hatakka, J., Eneroth, K., Kulmala, M., and Viisanen, Y.: Measurements of optical properties of atmospheric aerosols in Northern Finland, Atmos. Chem. Phys., 6, 1155–1164, doi:10.5194/acp-6-1155-2006, 2006. 32931, 32932, 32938

Anderson, T. and Ogren, J.: Determining aerosol radiative properties using the TSI 3563 integrating nephelometer, Aerosol Sci. Technol., 29, 57–69, 1998. 32928

Title Page

Abstract | Introduction

Conclusions | References

Tables | Figures

◄ | ►

◄ | ►

Back | Close

Full Screen / Esc

Printer-friendly Version

Interactive Discussion

Anderson, T., Covert, D., Marshall, S., Laucks, M., Charlson, R., Waggoner, A., Ogren, J., Caldow, R., Holm, R., Quant, F., Sem, G., Wiedensohler, A., Ahlquist, N., and Bates, T.: Performance characteristics of a high-sensitivity, three-wavelength, total scatter/backscatter nephelometer, J. Atmos. Ocean. Technol., 13, 967–986, 1996. 32928

Asmi, A., Wiedensohler, A., Laj, P., Fjaeraa, A.-M., Sellegri, K., Birmili, W., Weingartner, E., Baltensperger, U., Zdimal, V., Zikova, N., Putaud, J.-P., Marinoni, A., Tunved, P., Hansson, H.-C., Fiebig, M., Kiveks, N., Lihavainen, H., Asmi, E., Ulevicius, V., Aalto, P. P., Swietlicki, E., Kristensson, A., Mihalopoulos, N., Kalivitis, N., Kalapov, I., Kiss, G., de Leeuw, G., Henzing, B., Harrison, R. M., Beddows, D., O'Dowd, C., Jennings, S. G., Flentje, H., Weinhold, K., Meinhardt, F., Ries, L., and Kulmala, M.: Number size distributions and seasonality of submicron particles in Europe 2008–2009, Atmos. Chem. Phys., 11, 5505–5538, doi:10.5194/acp-11-5505-2011, 2011. 32930, 32933, 32935, 32936

Birmili, W., Wiedensohler, A., Heintzenberg, J., and Lehmann, K.: Atmospheric particle number size distribution in Central Europe: statistical relations to air masses and meteorology, J. Geophys. Res., 106, 32005–32018, 2001. 32925

Bond, T.: Spectral dependence of visible light absorption by carbonaceous particles emitted from coal combustion, Geophys. Res. Lett., 28, 4075–4078, 2001. 32926

Bond, T., Anderson, T., and Campbell, D.: Calibration and intercomparison of filter-based measurements of visible light absorption by aerosols, Aerosol Sci. Technol., 30, 582–600, 1999. 32928, 32929

Boucher, O. and Haywood, J.: On summing the components of radiative forcing of climate change, Clim. Dynam., 18, 297–302, 2001. 32924

Cappa, C., Bates, T., Quinn, P., and Lack, D.: Source characterization from ambient measurements of aerosol optical properties, Geophys. Res. Lett., 36, L14 813, doi:10.1029/2009GL038979, 2009. 32937

Clarke, A. and Noone, J.: Measurements of soot aerosol in Arctic snow, Atmos. Environ., 19, 2045–2054, 1985. 32924

Clarke, A., McNaughton, C., Kapustin, V., Shinozuka, Y., Howell, S., Dibb, J., Zhou, J., Anderson, B., Brekhovskikh, V., Turner, H., and Pinkerton, M.: Biomass burning and pollution aerosol over North America: organic components and their influence on spectral optical properties and humidification response, J. Geophys. Res., 112, D12S18, doi:10.1029/2006JD007777, 2007. 32937

Collaud Coen, M., Weingartner, E., Schaub, D., Hueglin, C., Corrigan, C., Henning, S.,

Schwikowski, M., and Baltensperger, U.: Saharan dust events at the Jungfraujoch: detection by wavelength dependence of the single scattering albedo and first climatology analysis, Atmos. Chem. Phys., 4, 2465–2480, doi:10.5194/acp-4-2465-2004, 2004. 32926

Delene, D. and Ogren, J.: Variability of aerosol optical properties at four North American surface monitoring sites, J. Aerosol Sci., 59, 1135–1150, 2002. 32931

Draxler, R. and Rolph, G.: (HYbrid Single-Particle Lagrangian Integrated Trajectory) Model access via NOAA ARL READY Website, NOAA Air Resources Laboratory, Silver Spring, MD, available at: http://www.arl.noaa.gov/ready/hysplit4.html, last access: 15 August 2011, 2003. 32940

Dubovik, O., Holben, B., Eck, T., Smirnov, A., Kaufman, Y., King, M., Tanré, D., and Slutsker, I.: Variability of absorption and optical properties of key aerosol types observed in worldwide locations, J. Atmos. Sci., 59, 590–608, 2002. 32926

Garland, R. M., Yang, H., Schmid, O., Rose, D., Nowak, A., Achtert, P., Wiedensohler, A., Takegawa, N., Kita, K., Miyazaki, Y., Kondo, Y., Hu, M., Shao, M., Zeng, L. M., Zhang, Y. H., Andreae, M. O., and Pöschl, U.: Aerosol optical properties in a rural environment near the mega-city Guangzhou, China: implications for regional air pollution, radiative forcing and remote sensing, Atmos. Chem. Phys., 8, 5161–5186, doi:10.5194/acp-8-5161-2008, 2008. 32939

IPCC: Climate Change 2007, Tech. rep., Intergovernmental Panel on Climate Change, Cambridge University Press, Cambridge, 2007. 32924

Kokhanovsky, A.: Aerosol Optics: Light Absorption and Scattering by Particles in the Atmosphere, Springer, Praxis, Bremen, Germany, 2008. 32923

Law, K. and Stohl, A.: Arctic air pollution: origins and impacts, Science, 315, 1537–1540, doi:10.1126/science.1137695, 2007. 32924

Leck, C. and Bigg, E.: Source and evolution of the marine aerosol – a new perspective, Geophys. Res. Lett., 32, L19803, doi:10.1029/2005GL023651, 2005. 32924

Li, Z., Xia, X., Cribb, M., Mi, W., Holben, B., Wang, P., Chen, H., Tsay, S.-C., Eck, T., Zhao, F., Dutton, E., and Dickerson, R.: Aerosol optical properties and their radiative effects in Northern China, J. Geophys. Res., 112, D22S01, doi:10.1029/2006JD007382, 2007. 32925

Lin, C., Baker, M., and Charlson, R.: Absorption coefficient of atmospheric aerosol: a method of measurement, Appl. Opt., 12, 1356–1363, 1973. 32928

Lyamani, H., Olmo, F., and Alados-Arboledas, L.: Light scattering and absorption properties of aerosol particles in the urban environment of Granada, Spain, Atmos. Environ., 42,

Title Page

Abstract | Introduction

Conclusions | References

Tables | Figures

|◄ | ►|

◄ | ►

Back | Close

Full Screen / Esc

Printer-friendly Version

Interactive Discussion

2630–2642, 2008. 32932

Mogo, S., Cachorro, V., Sorribas, M., de Frutos, A., and Fernández, R.: Measurements of continuous spectra of atmospheric absorption coefficients from UV to NIR via optical method, Geophys. Res. Lett., 32, L13 811, doi:10.1029/2005GL022938, 2005. 32926

Montilla, E., Mogo, S., Cachorro, V., and de Frutos, A.: An integrating sphere spectral system to measure continuous spectra of aerosol absorption coefficient, J. Aerosol Sci., 42, 204–212, doi:10.1016/j.jaerosci.2011.01.003, 2011. 32925, 32926, 32932

Pereira, S. N., Wagner, F., and Silva, A. M.: Seven years of measurements of aerosol scattering properties, near the surface, in the southwestern Iberia Peninsula, Atmos. Chem. Phys., 11, 17–29, doi:10.5194/acp-11-17-2011, 2011. 32926

Quinn, P., Miller, T., Bates, T., Ogren, J., Andrews, E., and Shaw, G.: A 3-year record of simultaneously measured aerosol chemical and optical properties at Barrow, Alaska, J. Geophys. Res., 107, 4130, doi:10.1029/2001JD001248, 2002. 32924

Quinn, P., Shaw, G., Andrews, E., Dutton, E., Ruoho-Airola, T., and Gong, S.: Arctic haze: current trends and knowledge gaps, Tellus, 59, 99–114, 2007. 32931

Ramanathan, V., Crutzen, P., Kiehl, J., and Rosenfeld, D.: Aerosols, climate, and the hydrological cycle, Science, 294, 2119–2124, doi:10.1126/science.1064034, 2001. 32924

Ricard, V., Jaffrezo, J.-L., Kerminen, V.-M., Hillamo, R., Sillanpaa, M., Ruellan, S., Liousse, C., and Cachier, H.: Two years of continuous aerosol measurements in Northern Finland, J. Geophys. Res., 107, 4129, doi:10.1029/2001JD000952, 2002a. 32924

Ricard, V., Jaffrezo, J.-L., Kerminen, V.-M., Hillamo, R., Teinilä, K., and Maenhaut, W.: Size distributions and modal parameters of aerosol constituents in Northern Finland during the European Arctic Aerosol Study, J. Geophys. Res., 107, 4208, doi:10.1029/2001JD001130, 2002b. 32924

Rodríguez, E., Toledano, C., Cachorro, V., Ortiz, P., Stebel, K., Berjón, A., Blindheim, S., Gausa, M., and de Frutos, A.: Aerosol characterization at the sub-Arctic site Andenes (69° N, 16° E), by the analysis of columnar optical properties, Q. J. Roy. Meteorol. Soc., doi:10.1002/qj.921, in press, 2011. 32925, 32933, 32938, 32940

Rolph, G.: Real-time Environmental Applications and Display sYstem (READY), NOAA Air Resources Laboratory, Silver Spring, MD, available at: http://www.arl.noaa.gov/ready/hysplit4.html, last access: 15 August 2011, 2003. 32940

Rosen, H., Hansen, D., Gundel, L., and Novakov, T.: Identification of the graphitic carbon component of source and ambient particulates by Raman spectroscopy and an optical

attenuation technique, in: Carbonaceous Particles in the Atmosphere, Lawrence Berkeley Laboratory, Berkeley, 229–232, 1979. 32926

Russell, P. B., Bergstrom, R. W., Shinozuka, Y., Clarke, A. D., DeCarlo, P. F., Jimenez, J. L., Livingston, J. M., Redemann, J., Dubovik, O., and Strawa, A.: Absorption Angstrom Exponent in AERONET and related data as an indicator of aerosol composition, Atmos. Chem. Phys., 10, 1155–1169, doi:10.5194/acp-10-1155-2010, 2010. 32926

Skatteboe, R.: ALOMAR: atmospheric science using lidars, radars and ground based instruments, J. Atmos. Terr. Phys., 58, 1823–1826, doi:10.1016/0021-9169(95)00173-5, 1996. 32927

Toledano, C., Cachorro, V., Berjón, A., Sorribas, M., Vergaz, R., de Frutos, A., Antón, M., and Gausa, M.: Aerosol optical depth at ALOMAR Observatory (Andøya, Norway) in summer 2002 and 2003, Tellus B, 58, 218–228, 2006. 32925, 32927

Toledano, C., Cachorro, V., de Frutos, A., Torres, B., Sorribas, M., and de la Morena, B.: Air mass classification and analysis of aerosol types at El Arenosillo (Spain), J. Appl. Meteorol. Clim., 48, 962–981, 2009. 32940

Tomasi, C., Vitale, V., Lupi, A., Carmine, C. D., Campanelli, M., Herber, A., Treffeisen, R., Stone, R., Andrews, E., Sharma, S., Radionov, V., von Hoyningen-Huene, W., Stebel, K., Hansen, G., Myhre, C., Aaltonen, C. W. V., Lihavainen, H., Hillamo, A. V. R., Ström, J., Toledano, C., Cachorro, V., Ortiz, P., de Frutos, A., Blindheim, S., Frioud, M., Gausa, M., Zielinski, T., Petelski, T., and Yamanouchi, T.: Aerosols in polar regions: a historical overview based on optical depth and in situ observations, J. Geophys. Res., 112, D16205, doi:10.1029/2007JD008432, 2007. 32932

Tunved, P., Nilsson, E., Hansson, H.-C., Ström, J., Kulmala, M., Aalto, P., and Viisanen, Y.: Aerosol characteristics of air masses in Northern Europe: influences of location, transport, sinks, and sources, J. Geophys. Res., 110, D07201, doi:10.1029/2004JD005085, 2005. 32925

Virkkula, A., Hillamo, R., Kerminen, V.-M., and Stohl, A.: The influence of Kola Peninsula, continental European and marine sources on the number concentrations and scattering coefficients of the atmospheric aerosol in Finnish Lapland, Boreal Env. Res., 2, 317–336, 1998. 32938, 32939

Virkkula, A., Ahquist, N., Covert, D., Arnott, W., Sheridan, P., Quinn, P., and Coffman, D.: Modification, calibration and a field test of an instrument for measuring light absorption by particles, Aerosol Sci. Technol., 39, 68–83, 2005. 32928, 32929

SSA in the ALOMAR station

S. Mogo et al.

Title Page

Abstract | Introduction

Conclusions | References

Tables | Figures

◄ | ►

◄ | ►

Back | Close

Full Screen / Esc

Printer-friendly Version

Interactive Discussion

Virkkula, A., Backman, J., Aalto, P. P., Hulkkonen, M., Riuttanen, L., Nieminen, T., dal Maso, M., Sogacheva, L., de Leeuw, G., and Kulmala, M.: Seasonal cycle, size dependencies, and source analyses of aerosol optical properties at the SMEAR II measurement station in Hyytiälä, Finland, Atmos. Chem. Phys., 11, 4445–4468, doi:10.5194/acp-11-4445-2011, 2011. 32940

Vrekoussis, M., Liakakou, E., Koçak, M., Kubilay, N., Oikonomou, K., Sciare, J., and Mihalopoulos, N.: Seasonal variability of optical properties of aerosols in the Eastern Mediterranean, Atmos. Environ., 39, 7083–7094, doi:10.1016/j.atmosenv.2005.08.011, 2005. 32932

Title Page

Abstract | Introduction

Conclusions | References

Tables | Figures

◄ | ►

◄ | ►

Back | Close

Full Screen / Esc

Printer-friendly Version

Interactive Discussion

Table 1. Evaluation of the overall ranges and median values of the absorption/scattering coefficients, the Ångström exponents and the single scattering albedo obtained from the data set measured at ALOMAR. P_x values are the x-th percentage of the considered parameter. The median value (P_{50}) is bolded.

		Mean	StD	Range	P_{25}	P_{50}	P_{75}
σ_s (Mm^{-1})	450 nm	7.31	4.79	0.29–31.24	3.63	**6.58**	9.55
	550 nm	5.41	3.55	0.25–23.21	2.76	**4.75**	7.12
	700 nm	4.08	2.84	0.19–18.95	2.09	**3.39**	5.32
α_s (450–750)		1.37	0.61	0.20–3.07	0.82	**1.36**	1.90
σ_a (Mm^{-1})	450 nm	0.45	0.33	0.14–2.72	0.24	**0.35**	0.53
	550 nm	0.40	0.27	0.13–2.28	0.23	**0.32**	0.48
	700 nm	0.36	0.23	0.12–1.92	0.21	**0.30**	0.43
α_a (450–750)		0.40	0.21	0.01–0.97	0.25	**0.39**	0.55
ω_0	450 nm	0.93	0.04	0.60–0.99	0.91	**0.94**	0.96
	550 nm	0.91	0.05	0.62–0.99	0.89	**0.92**	0.95
	700 nm	0.89	0.06	0.50–0.99	0.86	**0.90**	0.94
α_{ω_0} (450–750)		0.09	0.09	−0.11–0.95	0.02	**0.07**	0.14

Table 2. Arithmetic mean values of the concentrations in each size section. P_x values are the x-th percentage of the considered parameter. The median value (P_{50}) is bolded.

$(\#/cm^3)$	Mean	StD	P_{16}	P_{25}	P_{50}	P_{75}	P_{84}
N_{30-50}	258	355	27	45	**127**	315	449
N_{50}	469	516	81	126	**266**	615	892
$N_{100(accumulation)}$	183	209	34	61	**114**	224	317
N_{Aitken} (30–100 nm)	545	647	68	111	**308**	711	1023
$N_{nucleation}$ (10–30 nm)	549	1070	29	53	**185**	488	881
$N_{submicrometer}$ (10–390 nm)	1277	1563	190	291	**710**	1635	2376
$N_{micrometer}$ (> 500 nm)	1	1	0	1	**1**	2	3
N_{total} (> 3 nm)	2463	4251	293	500	**1175**	2895	4113
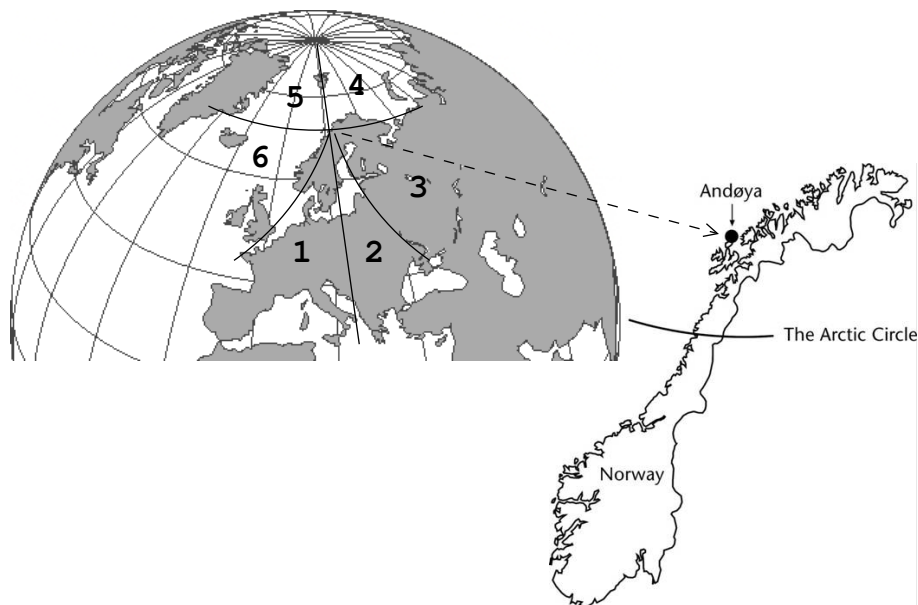
Fig. 1. Location of the ALOMAR station in Northern Norway. The classification sectors of back trajectories air masses are also displayed.

Printer-friendly Version

Interactive Discussion
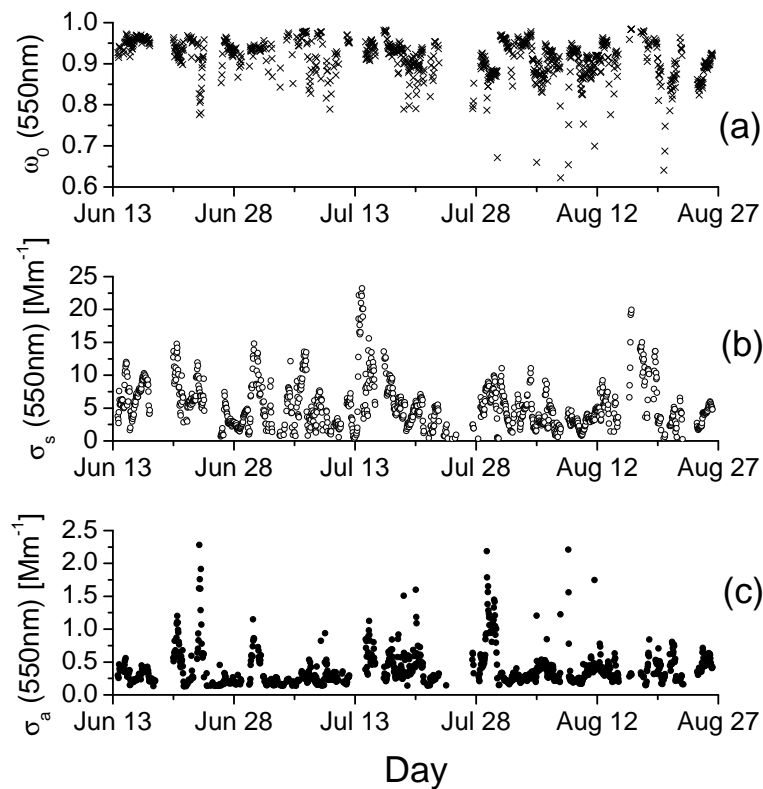
Fig. 2. Time-series of hourly average values of **(a)** single scattering albedo, **(b)** scattering coefficient and **(c)** absorption coefficient at 550 nm.
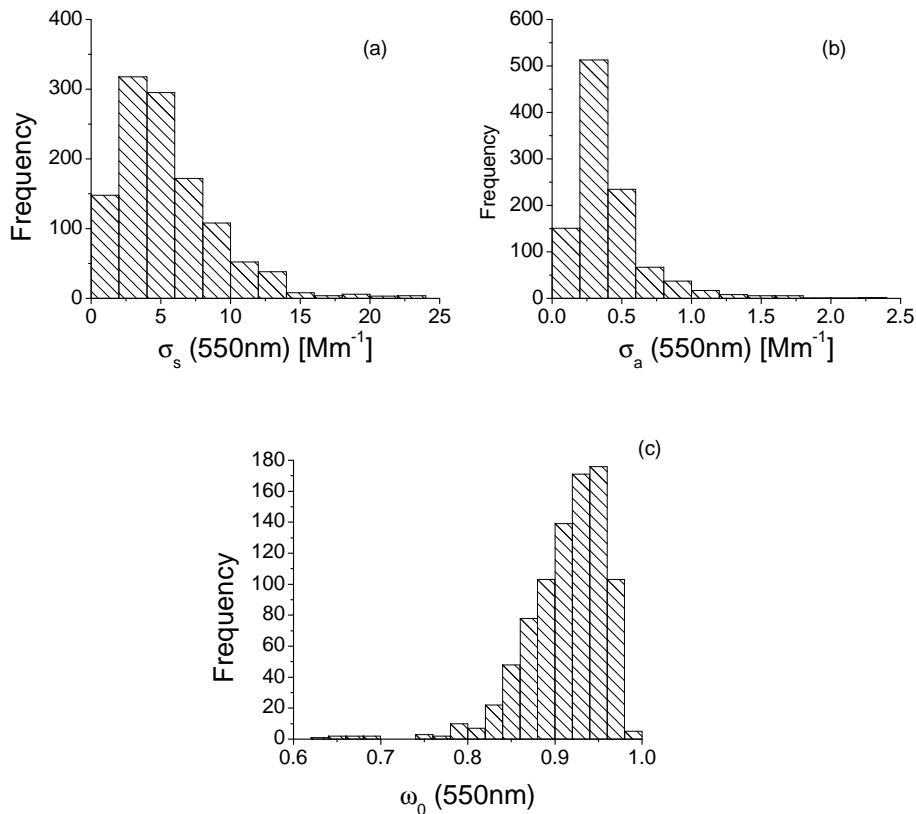
Fig. 3. Frequency histogram for the **(a)** scattering coefficient, **(b)** absorption coefficient and **(c)** single scattering albedo.

Discussion Paper | Discussion Paper | Discussion Paper | Discussion Paper |

ACPD

11, 32921–32964, 2011

SSA in the ALOMAR station

S. Mogo et al.

Title Page

Abstract | Introduction

Conclusions | References

Tables | Figures

|◀ | ▶|

◀ | ▶

Back | Close

Full Screen / Esc

Printer-friendly Version

Interactive Discussion
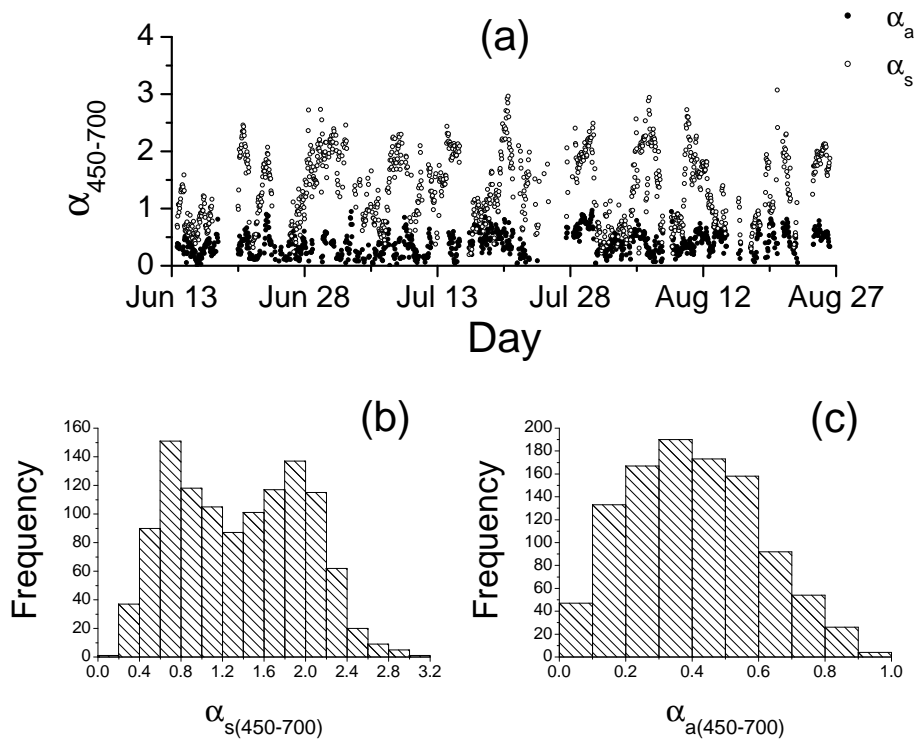
Fig. 4. (a) Time-series of hourly average values of the absorption/scattering Ångström exponents. **(b, c)** Frequency histogram for the scattering and absorption Ångström exponents.
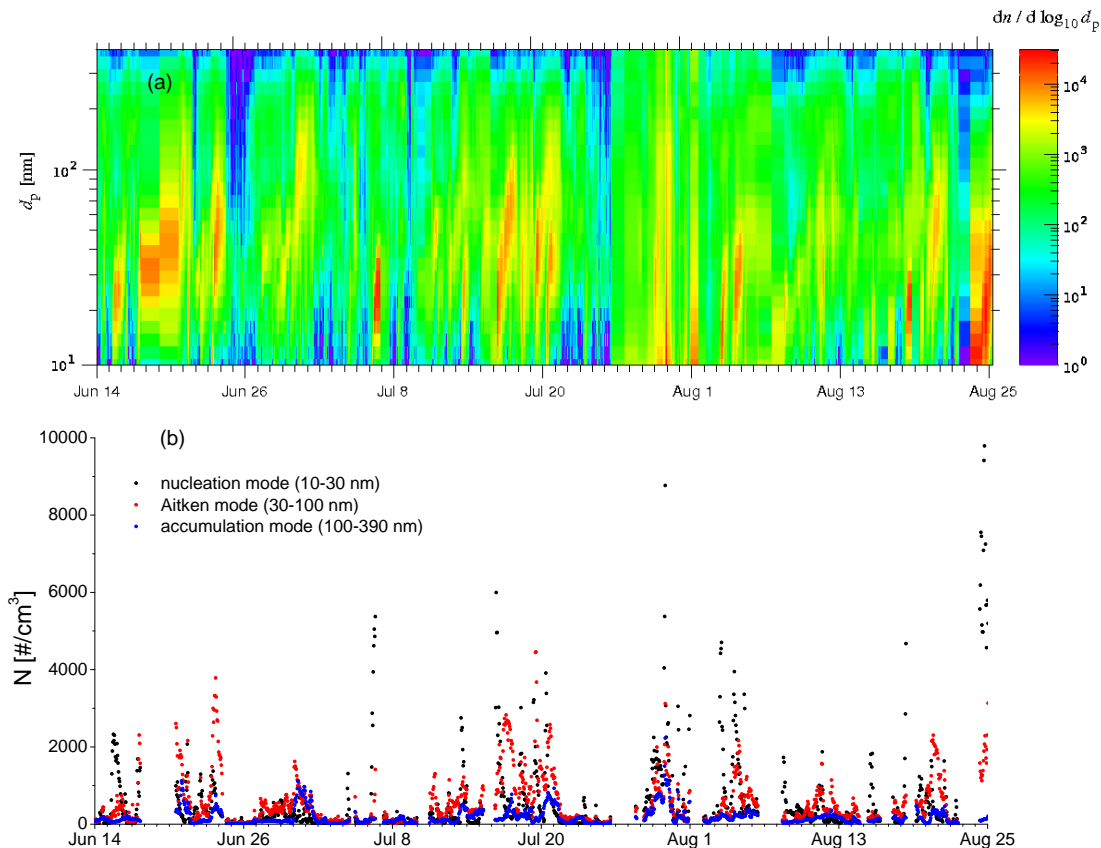
Fig. 5. **(a)** Particle number size distributions measured for the submicrometer particles. **(b)** Temporal variation of the concentration of nucleation, Aitken and accumulation modes.
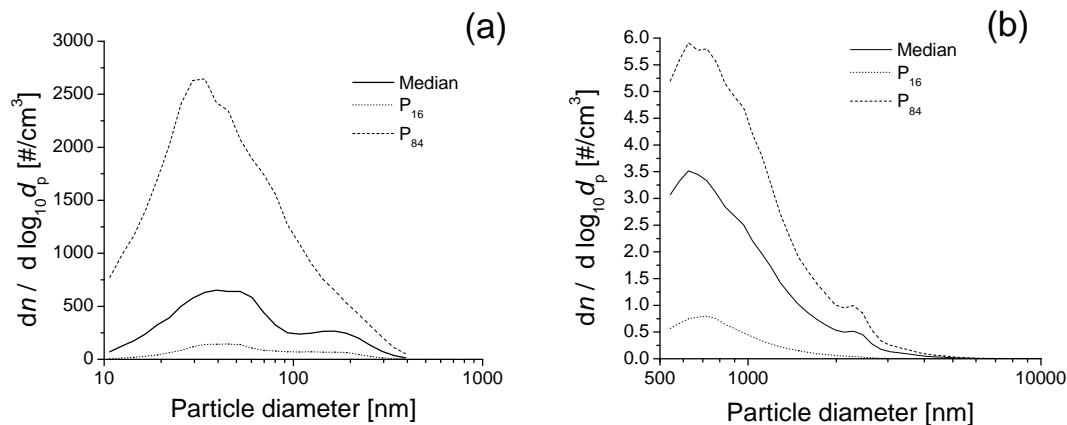
Fig. 6. Median distributions with the 16th and 84th percentile distributions for the: **(a)** submi-crometer particles, **(b)** micrometer particles.
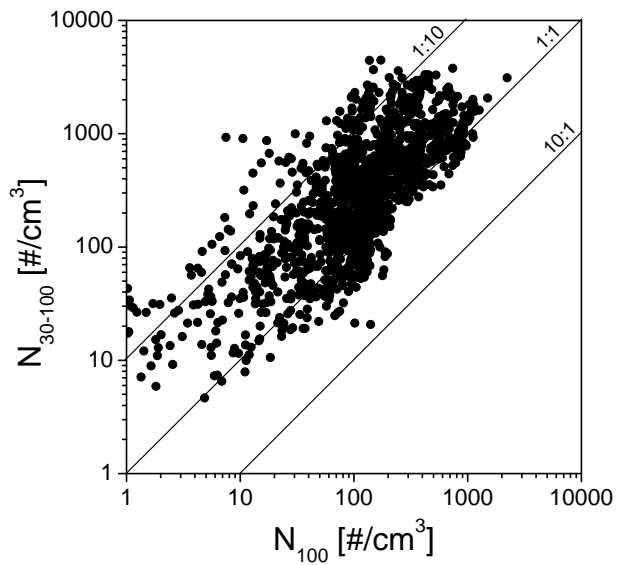
Fig. 7. Scatter plot of particle concentration between 30 and 100 nm as a function of particle concentrations above 100 nm.
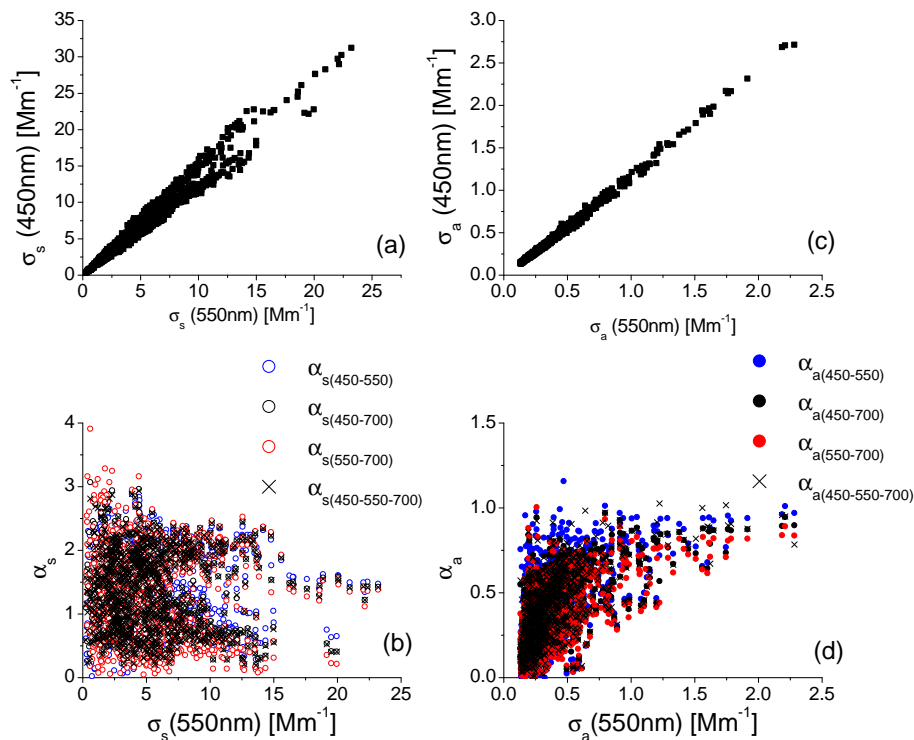
Fig. 8. Hourly average values of the **(a)** scattering and **(c)** absorption for different wavelengths. Hourly average values of the **(b)** scattering coefficient at 550 nm as a function of the scattering Ångström exponents and **(d)** absorption coefficient at 550 nm as a function of the absorption Ångström exponents.
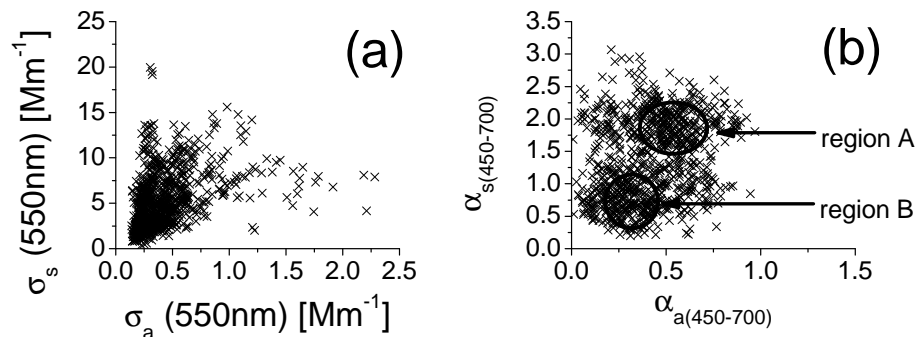
Fig. 9. Relationship between **(a)** the coefficients σ_s and σ_a, **(b)** the slopes α_s and α_a and **(c)** the single scattering albedo, ϖ_0, and its slope, α_{ϖ_0}.
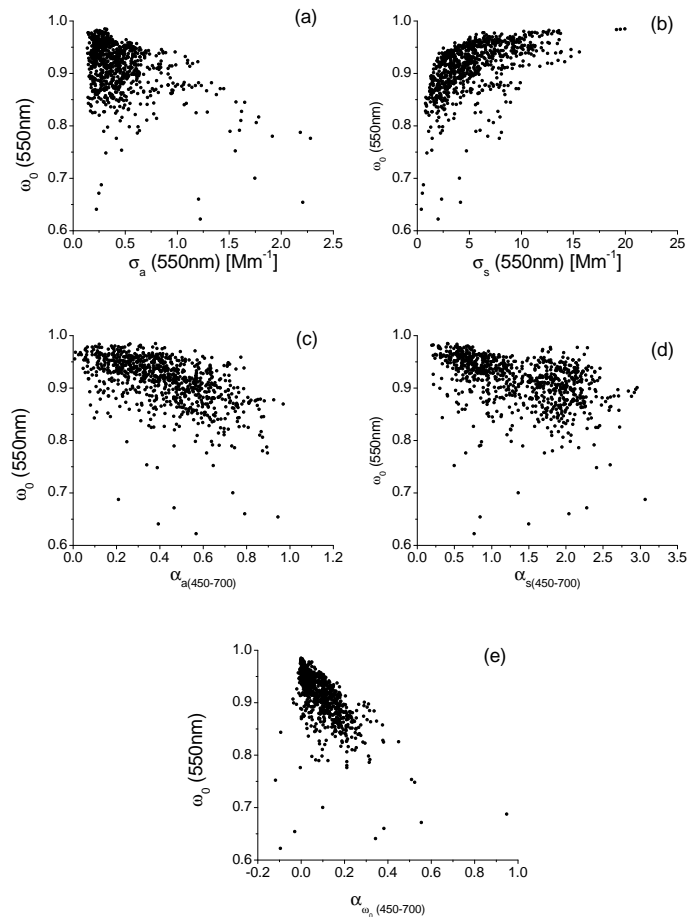
Fig. 10. Hourly average values of the single scattering albedo as a function of the **(a)** absorption coefficient, **(b)** scattering coefficient, **(c)** absorption Ångström exponent, **(d)** scattering Ångström exponent and **(e)** exponent α_{ω_0}.

Title Page

Abstract | Introduction

Conclusions | References

Tables | Figures

|◄ | ►|

◄ | ►

Back | Close

Full Screen / Esc

Printer-friendly Version

Interactive Discussion
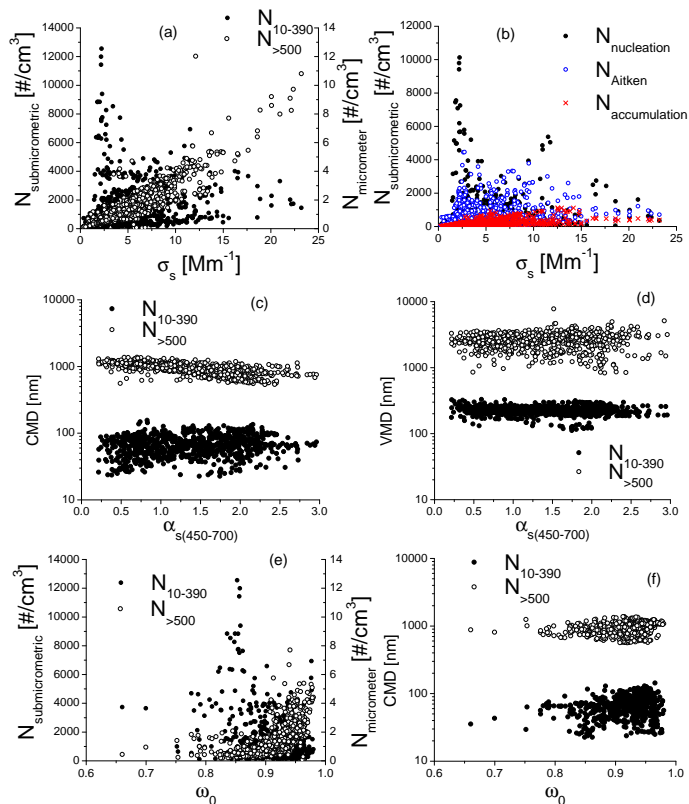
Fig. 11. Relation between σ_s and **(a)** micrometer and submicrometer concentrations, **(b)** nucleation, Aitken and accumulation modes. **(c)** Relation between the size of the particles (CMD) and α_s. **(d)** Relation between the size of the particles (VMD) and α_s. **(e)** Relation between ϖ_0 and the micrometer and submicrometer concentrations. **(f)** Particle size (count mean diameter) as a function of ϖ_0.
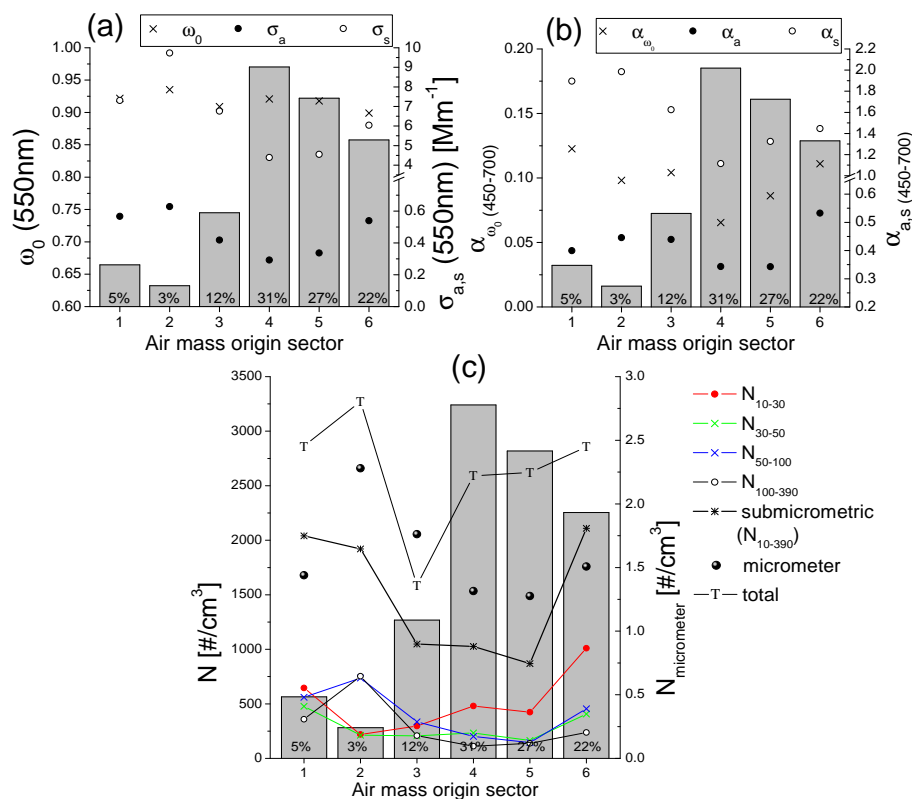
Fig. 12. Classification of air masses according to its origin and **(a,b)** optical parameters; **(c)** number concentrations observed in each situation. Percentage values refer the frequency of each air mass origin.
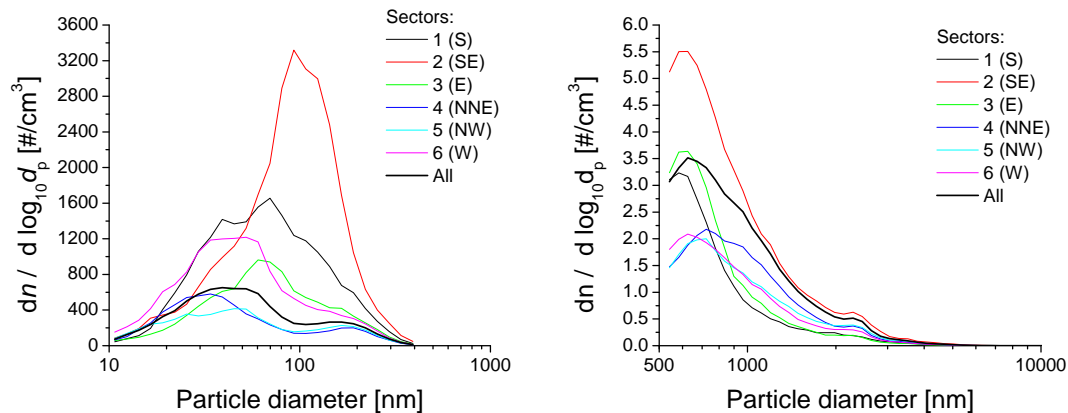
Fig. 13. Median size distributions observed in different air masses.